Relativistic electron generation in interactions of a 30 TW laser pulse with a thin foil target

G. Malka,* M. M. Aleonard,[†] J. F. Chemin, G. Claverie, M. R. Harston, and J. N. Scheurer
Centre d'Etudes Nucléaires de Bordeaux-Gradignan, 33175 Gradignan, France

V. Tikhonchuk
Institut de Physique Fondamentale, Université Bordeaux 1, 33175 Gradignan, France

S. Fritzler, V. Malka, P. Balcou, G. Grillon, S. Moustaizis, and L. Notebaert
ENSTA/LOA, 91128 Palaiseau, France

E. Lefebvre and N. Cochet
DPTA, CEA/DAM Ile de France, Boîte Postale 12, 91680 Bruyères-le-Châtel, France

Energy and angular distributions of the fast outgoing electron beam induced by the interaction of a 1 J, 30 fs, 2×10^{19} W/cm^2, 10 Hz laser with a thin foil target are characterized by electron energy spectroscopy and photonuclear reactions. We have investigated the effect of the target thickness and the intensity contrast ratio level on the electron production. Using a 6-μm polyethylene target, up to 4×10^8 electrons with energies between 5 and 60 MeV were produced per laser pulse and converted to γ rays by bremsstrahlung in a Ta secondary target. The rates of photofission of U as well as photonuclear reactions in Cu, Au, and C samples have been measured. In optimal focusing conditions, about 0.06% of the laser energy has been converted to outgoing electrons with energies above 5 MeV. Such electrons leave the target in the laser direction with an opening angle of 2.5°.

PACS number(s): 52.38.−r, 52.38.Kd, 25.20.Dc, 24.10.Lx

I. INTRODUCTION

Since the first observations of relativistic electrons generated by the interaction of high-intensity lasers with solids or thin foil targets [1–4], developments in laser technology have led to a large gain in the energy of emitted electrons from laser plasmas. It is now clearly established that the production of electrons with energy larger than 1 MeV requires a minimum laser intensity of 10^{18} W/cm^2. The electron distribution is quasi-Maxwellian, characterized by a hot electron temperature T_h which scales approximately as the square root of the laser intensity [1,5–7]. Temperatures $T_h \simeq 1$ MeV were obtained with a subpicosecond laser with incident energy of 20–50 J [1,8]. Temperature of the same order, $T_h = 2$ MeV, have been obtained at the Livermore laboratory with the petawatt laser in the 2 ps pulse regime at incident energies around 300 J [9]. Electron temperatures in the range of 5–10 MeV have only been obtained recently in the interaction of picosecond [10] and femtosecond lasers [11,12] with gas jet targets. It should be noted that these publications report approximately the same number of accelerated relativistic electrons per energy and per solid angle: about 10^{10} electrons per MeV and per steradian. This number is still significantly less than the number of electrons generated inside the target, as predicted by particle-in-cell simulations.

Several mechanisms have been proposed to explain the electron acceleration. They are acceleration by (i) the pon-

deromotive potential of the laser [5,6], (ii) fast plasma waves [7], and (iii) the laser field itself [13]. These mechanisms are not exclusive of each other. They coexist with their relative contributions depending strongly upon the particular experimental conditions. The main parameters affecting electron distributions are the laser parameters (the temporal and spatial distributions of the energy and wavelength), the nature of the target (gas, thin foil, or thick target), and the angle of incidence of the laser on the target. Previous experiments [3,14] have shown the importance of the formation of a preplasma in front of the target prior to the arrival of the energetic laser pulse, which then accelerates the electrons up to relativistic energies via the various mechanisms mentioned above.

Here, we present results obtained for the generation of high energy electrons escaping the target in the interaction of a 1 J, 30 fs, 10 Hz laser with thin polyethylene foils. The energy and angular distributions of the fast electron beam produced with different target thicknesses are characterized by electron energy spectroscopy and by photonuclear reactions.

II. EXPERIMENTAL METHODS

A. Laser characteristics

The experiment was carried out using the chirped pulse amplification (CPA) beam of the "salle jaune" Ti-sapphire laser system [15] at Laboratoire d'Optique Appliquée. The laser wavelength was 0.8 μm, the pulse duration was 30 fs, and the incident energy on the target was 1 J. The laser pulse was focused on to a 10-μm-diameter spot that included 50% of the energy, using an f/6 off-axis parabolic mirror. The

─────────
*Electronic address: malka@cenbg.in2p3.fr
[†]Corresponding author. Email address: aleonard@cenbg.in2p3.fr

laser was directed onto the target at normal incidence. The main 30-fs pulse was set on top of a long pedestal resulting from the amplified spontaneous emission (ASE). The delay between the beginning of the ASE and the main pulse could be adjusted from 1 ns to 2 ns. The intensity contrast ratio between the main pulse and the pedestal was $\approx 10^6 - 10^7$. From these numbers, assuming the same divergence, one deduces a typical intensity on a target of $(2 \pm 1)10^{19}$ W/cm^2 and $10^{12} - 10^{13}$ W/cm^2 for the main pulse and ASE, respectively. As a consequence, the main pulse interacted with a preplasma induced by the ASE pedestal. By adjusting the delay between the pulse and the beginning of the ASE pedestal, one can modify the length of the preplasma in front of the target. In this experiment, we did not record images of the preplasma and conclusions about its characteristics have been drawn from simulations and previous experiments.

B. Magnetic spectrometer

The energy distribution of the electrons exiting from the polyethylene target was measured with a magnetic spectrometer [16], which was installed behind the target at 0° with respect to the laser beam direction. The entrance of the spectrometer was defined by a 1-cm-diameter diaphragm mounted at 40 cm from the target defining a solid angle of 0.5 msr. The electrons were detected with five Si diodes. The output signals were analyzed by a digital oscilloscope. The full electron energy range between 5 MeV and 200 MeV was covered by changing the current intensity in the magnet. The number of electrons of a given energy detected in a diode was proportional to the voltage output.

C. Nuclear activation diagnostics

Nuclear activation in various elements was used to determine the total number of outgoing electrons emitted within a 42° half-angle cone with respect to the laser beam direction. This method selects electrons with an energy larger than the energy threshold of the photonuclear reaction involved. In a first step, the electron beam created in the plasma and escaping the target was incident on a 2-mm-thick Ta slab (converter) set a few millimeters behind the target. In the interaction, a significant part of the electron kinetic energy was converted into hard photons via the bremsstrahlung mechanism. In a second step, these photons induced photonuclear reactions in samples placed a few cm behind the converter. This nuclear diagnostic was used for measurements of the integrated flux of gammas, as well as for angular distribution measurements. The nuclear reactions used were ^{12}C$(\gamma,n)^{11}$C, ^{63}Cu$(\gamma,n)^{62}$Cu, ^{197}Au$(\gamma,n)^{196}$Au, and ^{238}U$(\gamma,$ fission). The activity measured in each sample was related to the angular and energy distributions of the photons and electrons using numerical simulations of particle interaction with the Monte Carlo code GEANT [17].

The high energy electron production was found to be very sensitive to the focalization and hence to the optimum production of a preplasma. To ensure the reproducibility of measurements, the target-converter assembly was made movable so that, for each new setup, the position of the CH target was adjusted with respect to the focus of the laser beam by opti-
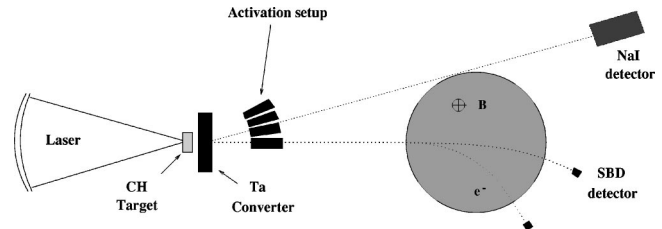

FIG. 1. Experimental setup.

mizing the electron counting rates in the spectrometer. With this precaution, a good reproducibility of activities produced in the samples was obtained. The γ activity of the samples was measured in a low noise area, either with two NaI detectors set in coincidence or with a Ge detector. These detectors were energy and efficiency calibrated with radioactive sources: ^{22}Na for the NaI detectors and ^{152}Eu for the Ge detector.

For the ^{12}C and ^{63}Cu samples, the β^+ radioactivity of ^{11}C and ^{62}Cu was measured by a coincidence technique using the two 511-keV γ rays emitted back-to-back after the positron annihilation. The samples were placed between two 2-mm-thick Pb foils to ensure a location of the annihilation close to the sample. In the case of ^{197}Au, the intensity of the 355-keV line in ^{196}Pt was measured with an intrinsic Ge γ-ray detector. In the case of ^{238}U, the γ rays emitted from the decay of selected isotopes (^{134}I, ^{89}Rb, ^{142}La) created in photofission reactions were detected [18]. Several laser shots were used for sample activation: 20 shots for Cu and C samples and up to 60 shots for the Au and U samples, where the decay half-life is not a limiting factor.

In order to monitor *in situ* the interaction efficiency, a 2×2 in.^{2} NaI scintillator was installed at 460 cm, viewing the laser-target interaction zone at an angle of 16° with respect to the laser beam directon. In nuclear activation measurements, the γ rays created in the tantalum slab reached the scintillator after passing through the 20-mm-thick aluminum walls of the vacuum chamber. The scintillator was shielded by 10-cm walls of lead, except in front of the entrance window where 5 cm of lead was used. The experimental setup is shown in Fig. 1.

D. Monte Carlo simulations of secondary processes

In order to find relations between the measured radioactive yield and the number of high energy electrons, we used the standard Monte Carlo particle code GEANT [17]. This code describes the propagation of high energy electrons and photons through the converter and the activation sample. The experimental setup was given as an input to the code. GEANT takes into account elastic and inelastic collisions, production of secondary particles, and their secondary processes. The standard code has been modified to include the nuclear photoexcitation processes. The energy differential cross section for each photonuclear reaction was taken from the references given in Table I. Since we were interested in the yield of photoactivation reactions with thresholds of 5.8 MeV and more, only electrons with energies larger than 5 MeV have been considered. 10^6 particles were used in simulations and

TABLE I. Number of nuclear reactions produced per laser shot in thick samples, set behind the 2-mm Ta converter and the 6-μm polyethylene target.

Reactions	$T_{1/2}$	Decay	Energy threshold (MeV)	Thickness sample (cm)	Observation angle α [a]	Experimental number of reactions per shot	Number of reactions per electron from GEANT	Cross section reference
^{12}C$(\gamma,n)^{11}$C	20.4 mn	β^+	18.	0.8	26°	0.7×10^3	27×10^{-7}	[20]
^{63}Cu$(\gamma,n)^{62}$Cu	9.7 mn	$\beta+$	9.7	0.4	42°	9×10^3	29×10^{-6}	[21]
^{197}Au$(\gamma,n)^{196}$Au	6.18 d	γ	8	0.2	40°	5×10^4	92×10^{-6}	[22]
^{238}U(γ,f)	[b]	γ	5.8	0.2	22°	2.3×10^4	40×10^{-6}	[23]

[a]α is the half-angle aperture seen from the converter.
[b]$T_{1/2}$ depends on the fission product, see text.

the initial distribution of outgoing electrons was approximated by a Maxwellian distribution in energy and a Gaussian angular distribution

$$d^2N_e/dEd\Omega = N_o e^{(-E/T_h)} e^{(-\theta^2 \ln 2/\langle\theta_e\rangle^2)}, \qquad (1)$$

which is a good approximation to our experimental results. The temperature of hot electrons, T_h, was taken from the spectrometer measurements of the electron distribution at 0° and the mean divergence angle $\langle\theta_e\rangle$ has been adjusted to fit the observed angular divergence of photons in the activated samples. In order to obtain enough statistics from simulations within a reasonable computation time, the nuclear cross section was multiplied by a factor of 100.

Typical spectra of photons after the converter and in the activation sample are shown in Fig. 2. In this example corresponding to the Cu sample, only photons with energies above the 10-MeV threshold contribute to the activation. The largest contribution to the yield comes from electrons above twice the reaction threshold, and the contribution decreases at larger energy, due to the smaller electron number. The calculated number of reactions was used to find the number of outgoing electrons assuming a linear relation between the number of primary electrons and the radioactive yield.

III. EXPERIMENTAL RESULTS

We have investigated the production of fast electrons by varying the CH target thickness and the focusing conditions of the laser beam. Thin foils were mounted on a 70-μm-thick Ni grid. The diameter and spacing of the holes in the grid were 1 mm and 2 mm, respectively. After each laser shot, the target assembly was moved.

A. Outgoing electron energy distribution measurements

Figure 3 (top) shows the number of electrons escaping the target, N_e, per energy unit (MeV) and per solid angle unit (sr) measured at 0° with the spectrometer. The targets were polyethylene films with a thickness of 2, 6, and 100 μm. The laser contrast ratio was set at its maximum value and the delay between the main pulse and the pedestal was 2 ns for all three cases. The error bars result from an average of three consecutive measurements made in the same conditions. The

experimental energy distributions have been fitted with the energy dependence of the Maxwellian distribution given in Eq. (1), characterized by a hot temperature T_h.

Large differences were seen in the distributions depending on the target thickness. The 6-μm-thick target produced electrons with energies up to 70 MeV, at the limit of sensitivity of the spectrometer, with a temperature $T_h=(9.3\pm0.9)$ MeV and $N_0=(9\pm1)\times10^9 e/(\text{MeV sr})$. A very similar distribution was observed with an 11-μm-thick target. We noticed in each case a dependence on the delay between the beginning of the pedestal and the femtosecond pulse. The largest delay, which can be correlated to the largest pre-
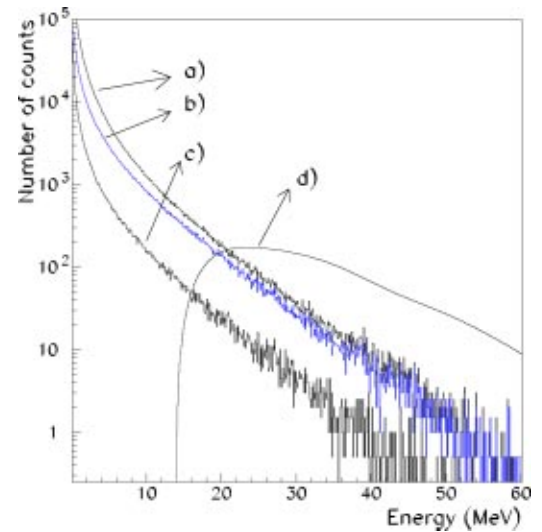

FIG. 2. GEANT simulation of the bremsstrahlung photons (in counts per 100 keV bins in the photon energy) and photonuclear reactions produced in a 4-mm-thick ^{63}Cu sample in the experimental geometry described in the text. The simulation is based on 10^6 electrons with energies larger than 5 MeV incident on the 2-mm Ta converter. Curves (a) and (b) are, respectively, the energy distributions of the bremsstrahlung photons generated in the Ta converter and of the photons reaching the Cu sample. Curve (c) shows the energy distribution of the photons created directly in the Cu sample by the electrons which have not been stopped in the Ta. Curve (d) gives the energy distribution of incident electrons which have produced the photonuclear reactions (the data have been multiplied by a factor of 100, see text).
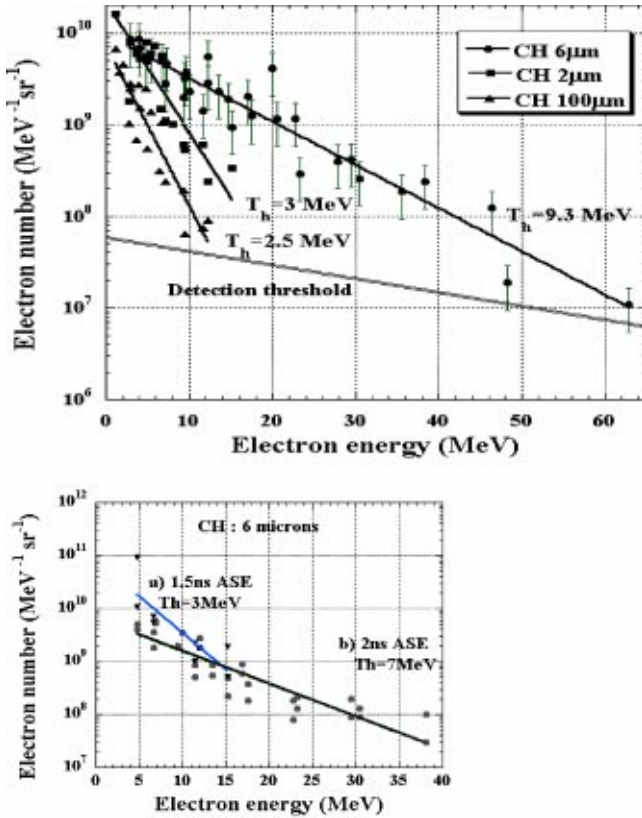
FIG. 3. Experimental electron energy distributions measured at $0°$, with an electron spectrometer with an aperture of 0.5 msr. Polyethylene (CH) targets are of 2, 6, and 100 μm thickness. The lines result from exponential fits to experimental data. Top: the hot electron temperatures are, respectively, (2.5 ± 0.2), (9.3 ± 0.9), and (3.0 ± 0.3) MeV. For the 2- and 100-μm target, error bars on the electron number measurements have not been drawn for the sake of clarity. Bottom: comparison with a 6-μm target for (a) 1.5-ns and (b) 2-ns delays in the ASE.

plasma length, produced the fastest electrons (delay of 2 ns), as is shown on Fig. 3 (bottom) for a 6-μm CH target. For the shown cases, the contrast ratio was not set at its maximum value. This is why we observed a smaller temperature ($T_h = 7$ MeV) for the 2-ns delay than indicated in the top figure.

For the 2-μm-thick target, the number of fast electrons decreases steeply with energy. The corresponding temperature was only $T_h=(3.0\pm0.3)$ MeV, that is, much less than for the 6-μm foil. The ablation rate of polyethylene in laser-plasma interactions at an intensity of 10^{13} W/cm^2 (the intensity of the focused prepulse) is of the order of 1 μm per ns [19]. In this case, the target is fully exploded before the arrival of the main femtosecond pulse, hence leading to a plasma density that is too low to produce a large number of fast electrons and to accelerate them to high energies. We obtained identical results with a 1-μm-thick target, independent of the delay between the pedestal and the main pulse.

Figure 3 (top) shows the results for a 100-μm-thick target. One sees that the number of electrons measured in the energy range from 10 to 20 MeV is very small compared to the 6-μm case. The temperature deduced from the data, $T_h=(2.5\pm0.3)$ MeV, is very similar to the 2-μm target case,

though the ablation of the target before the arrival of the femtosecond pulse can no longer be invoked in this case to explain the small number of fast electrons. The preplasma length and density should be almost the same as in the 6-μm case. Therefore some mechanism, acting on the electron trajectories between their acceleration at the front side of the target and the entrance in the spectrometer, has to be found to explain the electron energy distribution generated in the interaction of the laser with this thick CH target. This will be discussed further in relation with activation measurements.

B. Nuclear photoexcitation measurements: Activation

Using known values of photonuclear reaction cross sections, the integrated number of reactions induced in various samples can be used to determine the absolute number of electrons escaping from the target with an energy larger than the reaction threshold energy. Table I gives the list of photonuclear reactions used, the type of detected radioactivity, the half-lives of the reaction products, the reaction energy thresholds, and the thicknesses of the samples used. The measurements of activities induced in large copper slabs ($0.4\times1.9\times1.9$ cm^3), placed at 1 cm from the Ta converter and covering an angular range of $\pm42°$ with respect to the laser beam direction, gave a value for N_r, the number of reactions produced per laser shot (averaged over a few sets of 20 consecutive shots), of $N_r=(9000\pm2000)$ reactions per shot.

The experimental numbers of reactions per laser pulse induced in the C, Au, and U samples are reported in Table I. The smaller number of reactions found with the C sample is due to the larger energy threshold and the smaller photoexcitation cross section. We used the GEANT code to simulate the response of the experimental setup to a flux of electrons [17]. The incident electron energy dependence was given by Eq. (1) with the temperature $T_h=9.3$ MeV (measured for the 6-μm target with the magnetic spectrometer at $0°$ with respect to the laser direction). The converter was a 2-mm-thick piece of Ta.

Assuming a needlelike electron beam without angular divergence ($\langle\theta_e\rangle=0°$), we have drawn in Fig. 2, the energy distributions of the bremsstrahlung photons generated in the Ta converter (a), and of those reaching the Cu sample (b). Electrons are passing through the converter, and curve (c) represents the energy distribution of the photons created directly in the Cu sample by these electrons which have not been stopped in Ta. However, the number of such electrons is small as well as their contribution to the photon spectrum. Curve (d) gives the energy distribution of the incident electrons which have contributed to the photonuclear reactions. This curve clearly shows the importance of electrons with energies much higher than the peak energy (20 MeV) of the nuclear cross section. The same type of simulation has been performed with the other reactions. The number of nuclear reactions predicted in the simulations per incident electron is given in Table I.

The normalization of the measured reaction yields to the simulation results allows us to evaluate the number of outgoing electrons, N_e, with energies above the reaction thresh-

old in the experiment. From the results obtained in the photoactivation of Cu, we obtain $N_e = (3.1 \pm 0.8) \times 10^8$ electrons.

This number allows us to estimate the solid angle of the electron emission from the target, assuming that they have a smooth angular distribution with the maximum in the laser beam direction. Integrating the electron energy distribution, Eq. (1), over the energies above the minimum energy of 5 MeV used in GEANT simulations and using $T_h = 9.3$ MeV and $N_0 = 9 \times 10^9$ e/(MeV sr) obtained with the spectrometer one finds

$$dN_e/d\Omega = (5.4 \pm 0.9) \times 10^{10} e^{(-\theta^2 \ln 2/\langle \theta_e \rangle^2)} e/\text{sr}.$$

Combining these two values, we obtain the mean solid angle value

$$\Delta\Omega = \pi \langle \theta_e \rangle^2 = (6 \pm 2) \text{ msr}$$

for the emission of electrons from the polyethylene target with an energy larger than 5 MeV. This solid angle corresponds to a mean opening angle of the electron beam:

$$\langle \theta_e \rangle = (2.5 \pm 0.4)^\circ.$$

Similar results, within the error bars, were obtained with other photonuclear reactions, using the experimental and calculated results reported in Table I.

We also measured the activation of the copper sample in interactions with the 100-μm polyethylene target. The number of radioactive ^{62}Cu nuclei in the sample, per laser shot, dropped from ≈ 9000 to 2000.

C. Angular distribution measurements of the nuclear photoexcitation

The activation technique allows also direct measurements of the angular distribution of the emitted electrons. Following Refs. [8,9,24,25], the Ta slab, acting as a converter of electron kinetic energy into hard photons, was surrounded by copper wedges (see Fig. 1). The copper pieces were 5 mm thick (transverse direction), 1 cm in depth along the laser direction, and 1 cm high. The angle covered by each wedge was 6°. In order to obtain enough statistics in the counting of the radioactivity in each piece, we used 60 laser shots at a 1-Hz repetition rate with 6-μm- and 100-μm-thick polyethylene targets. The time delay induced by the 60 lasers shots (≈ 1 min) was of little influence on the decay of the 9.7 min half-life ^{62}Cu isotope. The data were corrected for the exact time delay between the beginning of the irradiation and the start of counting the activity.

The results of the photon angular distribution measurement are given in Fig. 4. The vertical errors bars are statistical uncertainties added quadratically to the systematic error in the detection efficiency. The horizontal bars give the angular resolution of the measurement. A fit of the experimental data points with a Lorentzian curve for the 6-μm target gives a full width at half maximum (FWHM) angle for the photon angular distribution of

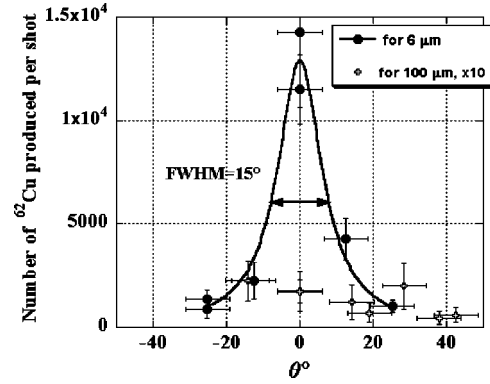$$(15 \pm 3)^\circ \Rightarrow \langle \theta_\gamma \rangle = (7.5 \pm 1.5)^\circ$$

FIG. 4. Number of ^{63}Cu$(\gamma,n)^{62}$Cu reactions produced per shot using 6- and 100-μm thick polyethylene targets versus the angular position of the 10-mm-thick Cu samples. The angular resolution is 6°.

and a mean direction of photons centered on the laser direction. This angular distribution only concerns the bremsstrahlung photons with energies between 10 MeV (the energy threshold of the reaction) and 25 MeV, above which the (γ,n) cross section is very small. The relation between the angular distributions of photons and electrons was established by GEANT simulations. Different electron beam angular distributions were tried as an input to finally reproduce the experimental activity in the different copper wedges.

The measured angular divergence of the electron beam found for the 6-μm target is in agreement with the value deduced from the integral measurement, if we take into account the limitation due to the finite angular resolution of the experiment. Indeed, for a needlelike electron beam without divergence, GEANT predicts that the bremsstrahlung photons would be emitted with a mean angular divergence $\langle \theta_\gamma \rangle = 8^\circ$. Increasing the angular divergence of the incident electron beam up to $\langle \theta_e \rangle = 3^\circ$ increases the value of $\langle \theta_\gamma \rangle$ to 9°.

For the 100-μm polyethylene target, the activity is distributed almost uniformly between different wedges. This demonstrates that the angular distribution of photons, and therefore, the fast electrons, is much wider than in the 6-μm case. The photon angular divergence is estimated to be $\langle \theta_\gamma \rangle = 30^\circ$. Fast electrons were not observed in the spectrometer with the 100-μm target, because the number of electrons emitted within the angular acceptance of the spectrometer was below the sensitivity threshold, due to the angular spreading and the deceleration of the electrons.

D. Reproducibility of the measurements

Figure 5 shows the decay of ^{62}Cu for different series of shots (6 μm polyethylene target). We found little variation (20%) in the measurements spaced over several days, indicating that the laser-plasma interaction was reproducible. On the other hand, the experiments carried out with the electron spectrometer demonstrate larger random deviations. The distribution of the diode pulse amplitudes shows a dispersion from shot to shot, which is much larger than 20%. Similar large fluctuations were reported in Ref. [8].

Our interpretation of this result is as follows. For the nuclear activation measurements, all the fast electrons exit-
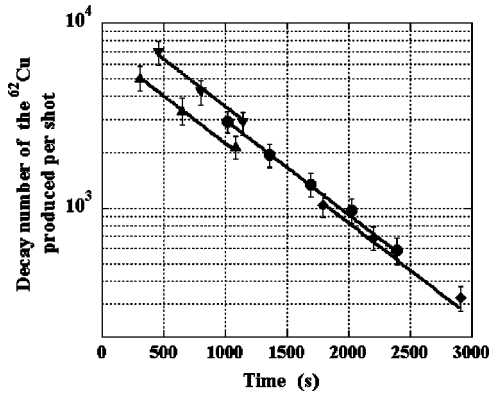
FIG. 5. Number of ^{63}Cu$(\gamma,n)^{62}$Cu reactions produced per shot in a 4-mm-thick Cu sample, using a 6-μm polyethylene target, versus β^+ time decay for four different runs of 60 shots each. The decay is in agreement with a half-life of ^{62}Cu of 9.7 min. The extrapolation at time $t=0$, gives the number of ^{63}Cu$(\gamma,n)^{62}$Cu reactions produced per shot equal to 9000 ± 2000.

ing from the polyethylene target reach the Ta converter, and in this case, the total number of bremsstrahlung photons remains the same from shot to shot, even if small angular deviations in the electron beam directions appear. On the other hand, in the electron energy distribution measurements, small deviations, of the order of 1° in the electron beam direction, are sufficient to prevent a large fraction of the electrons from entering the spectrometer. The consequence is that the signal amplitude from the spectrometer varies significantly. The more focused the electron beam, the larger the fluctuations of the electron distribution measurement with the spectrometer.

IV. DISCUSSION

The laser ASE emission, with an intensity of about 10^{13} W/cm^2 and duration of 1–2 ns, created a preplasma on the target surface. The characteristics of this preplasma were not measured directly in the experiment but they can be estimated from hydrodynamic simulations with codes used to model the interaction of nanosecond laser pulses with matter. According to these simulations, the 1-μm polyethylene foil becomes transparent to the laser radiation after 1 ns. At this time, the plasma, with a density of the order of 10^{19} cm^{-3} and an electron temperature of 400–500 eV, expands to a distance of about 100 μm from the foil. These parameters could be considered as typical for our preplasma. They will not be strongly modified after the arrival of the main pulse because its duration is very short compared to the ion density deformation [26].

The fully electromagnetic, relativistic particle-in-cell (PIC) code CALDER [27] has been used to compute the energy and angular distributions of the electrons produced during the interaction of the main 30-fs laser pulse with the preplasma and the target plasma. The simulations have been carried out in two-dimensional (2D) geometry, at intensities $(2-4)\times10^{19}$ W/cm^2 with the laser pulse normally incident on the target. The laser intensity spatial distribution had a Gaussian transverse shape with 6 μm FWHM. The pre-

plasma was accounted for by an exponential density ramp with a characteristic length of 13 μm and a total length of nearly 80 μm. The transverse system size was 26 μm, and 69×10^6 particles of each species (electrons and ions) were used to sample the plasma. Two types of plasma profiles were considered. The first one corresponded to targets that are fully exploded by the prepulse, with a maximum density of the exponential ramp varying from 0.4 to 1.1 times the critical density. The second one corresponded to targets that remain overcritical at the time of the main pulse arrival: here, the exponential density ramp stopped at a density of $0.6n_c$ and was followed by a slab of 2-μm $10n_c$ overdense plasma.

The PIC simulation can shed some light on the acceleration mechanism inside the plasma. The pulse propagates through the first 50 μm of the plasma with very little modification. A large amplitude electron plasma wave is excited behind the pulse, but it does not reach wave breaking, so that little electron heating is obtained. Yet around $0.1n_c$, some part of the laser pulse self-focuses dramatically and reaches twice its initial intensity in a one-wavelength-wide hot spot. Much stronger longitudinal electric fields are excited in the region of the target above $0.1n_c$, but they show very little coherence. Half of the pulse energy is rapidly absorbed at that time. Note that the resulting electron temperature is substantially higher than the ponderomotive potential of the incident laser pulse, which is less that 3 MeV, even when corrected for the effect of self-focusing. From $0.1n_c$ on, the pulse creates a magnetized, 6-μm-wide channel, where the time averaged B_z field is larger than 1500 T. The separation of electron acceleration between longitudinal and transverse electric field contributions, as done in Ref. [28], indicates a small contribution from longitudinal fields and appears consistent with an acceleration mechanism akin to direct laser acceleration [13]. This is also consistent with the observation of magnetized channels, and the fact that most of the absorption takes place in the high-density region of the target.

The electron distributions simulated at 0°, 8°, and 16° within $\pm2°$ (the numerical diagnostic resolution) along the laser axis are presented in Fig. 6 for the case of an exponential plasma with a maximum density of $0.6n_c$, irradiated at 4×10^{19} W/cm^2. The 0° electron distribution is directly comparable to the experimental electron distribution measured at 0° with the spectrometer for the 6-μm target (Fig. 3, top). There is an excellent agreement as regards the temperature (10 MeV) and the electron number above 5 MeV (6.4×10^{10} sr^{-1}).

However there remain some apparent differences between the simulations and observations. The rather sharp energy cutoff in the electron spectrum around 40 MeV was not observed in experiments. This may be due to the underestimation of self-focusing in our 2D simulations, rather than from the limited plasma length that we simulate, as most of the absorption seems to be localized between $0.1n_c$ and $1n_c$. Another significant difference concerns the number of accelerated electrons and their angular divergence. The total calculated number of electrons per pulse, with an energy larger than 5 MeV, is of the order of 3×10^9 within a 42° cone, ten times more than the number found in the activation measurements. This difference cannot be explained by the trapping of
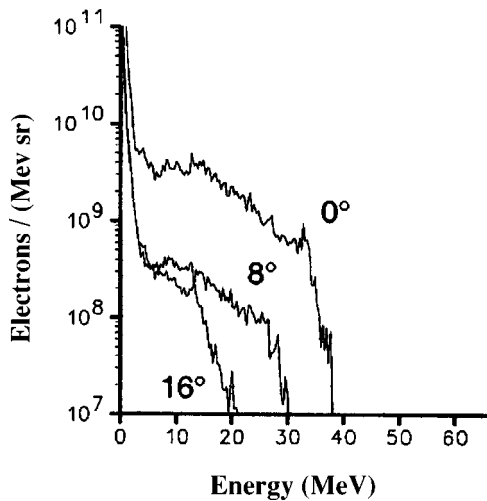
FIG. 6. Electron energy distribution per energy and solid angle unit as calculated in a PIC simulation, at 0°, 8°, and 16° from the laser direction.

the accelerated electrons by the space charge around the solid target. The escaped electrons with energy more than 5 MeV would charge the target to the potential $\Phi = eN_e/2\pi\epsilon_0 d \simeq 100$ kV (assuming the emission diameter $d = 10$ μm and taking the measured total number of fast electrons $N_e = 3 \times 10^8$), which is much smaller than their energy. The electrons with smaller energies (which have not been measured with our activation diagnostics) cannot charge the plasma to a potential higher than their energy. Therefore one should believe that the number of accelerated electrons in the experiment is somewhat less than predicted. It is important to note that our 2D code cannot compute actual electron numbers, but only linear densities. We convert them into dimensionless numbers by multiplying by a characteristic transverse length of the problem, taken to be the incident pulse FWHM, 6 μm. As we observed that most of the pulse absorption takes place after a strong self-focusing, we may actually overestimate the characteristic length and hence the electron number. Future 3D simulations can confirm this explanation.

When the interaction takes place at lower intensity, or with a higher plasma density, the calculated electron distribution was somewhat colder. Interestingly, it was also colder for the lowest plasma density of $0.4n_c$, thus supporting the experimental observation of a low electron temperature for the thinnest targets (2 μm).

Another important observation, which needs to be explained, is the effect of the target thickness on the fast electron characteristics. According to the recent estimates of the interaction of the relativistic electrons with dielectrics [29],

the density of the fast electron beam, which is about 3×10^{17} cm^{-3} (assuming the beam duration of 30 fs and diameter of 10 μm), is not sufficient for producing collective effects. However, it was seen in PIC simulations and has also been measured in other experiments that the generation of a high energy electron beam is accompanied by the production of a much larger number of mildly relativistic electrons, with energies of the order of the ponderomotive potential (1 MeV or less). These electrons have a much wider angular distribution, and their density can be of the order of the critical density. In very thin targets of the order of 10 μm, these two electron populations do not mix, because the lower energy component is trapped around the target by the space charge. Entering the dielectric layer placed behind the plasma (unionized part of the target), these ponderomotively accelerated electrons ionize it by their self-consistent electric field, compensate their space charge, and propagate along with the fast electron beam. The electric and magnetic fields created in the process of ionization and generation of the return current may affect the propagation of the fast electron beam. According to Ref. [29], the ionization of the dielectric partially screens the electric field of hot electrons and saturates it at the level of about 10% of the atomic electric field, that is, at the level of about 500 MV/cm. This electric field also generates a magnetic field evolving in the pulse duration time scale of 30 fs. Such a field is of the order of 100 T. It corresponds to a cyclotron radius of several hundred μm, which will strongly affect the electron trajectories. At the same time, the electric field of 500 MV/cm at the target thickness of 100-μm will decrease the electron energy up to 5 MeV. These two effects are probably responsible for the degradation of the fast electron characteristics in the case of the thick 100-μm polyethylene target.

V. CONCLUSIONS

We have characterized the energy and angular distributions of high energy outgoing electrons produced in the interaction of a 1 J, 30 fs laser pulse with thin CH foil targets, by measuring the electron energy either with a spectrometer or with photonuclear reactions. We have shown that the interaction of a 1-J CPA laser with a 6-μm polyethylene target produces an electron beam of 3×10^8 electrons, collimated within 2.5°, with energies between 5 and 60 MeV, and 9.3 MeV temperature. This electron production is comparable [9–12] with electron energy distributions obtained in other laser–solid target interaction experiments. Though only 0.06% of the laser energy was converted into outgoing electrons with energies above 5 MeV, our experiments demonstrate that femtosecond laser pulses are more efficient at generating energetic electrons than higher energy picosecond pulses.

[1] C. Darrow *et al.*, Proc. SPIE **1860**, 46 (1993); G. Malka and J.L. Miquel, Phys. Rev. Lett. **77**, 75 (1996); G. Malka *et al.*, *ibid.* **79**, 2053 (1997).

[2] S. Bastiani *et al.*, Phys. Rev. E **56**, 7179 (1997).

[3] S. Bastiani *et al.*, Phys. Rev. E **60**, 3439 (1999).

[4] K.B. Wharton *et al.*, Phys. Rev. Lett. **81**, 822 (1998).

[5] S.C. Wilks *et al.*, Phys. Rev. Lett. **69**, 1383 (1992).

[6] E. Lefebvre *et al.*, Phys. Rev. E **55**, 1011 (1997).

[7] T. Tajima and J.M. Dawson, Phys. Rev. Lett. **43**, 267 (1979).

[8] P.A. Norreys *et al.*, Phys. Plasmas **6**, 2150 (1999); K.W.D. Ledingham *et al.*, Phys. Rev. Lett. **84**, 899 (2000).

[9] T.E. Cowan *et al.*, Nucl. Instrum. Methods Phys. Res. A **455**, 130 (2000); Phys. Rev. Lett. **84**, 903 (2000).

[10] A. Modena *et al.*, Nature (London) **377**, 606 (1995).

[11] C. Gahn *et al.*, Phys. Plasmas **9**, 987 (2002).

[12] V. Malka *et al.*, Phys. Plasmas **8**, 2605 (2001).

[13] A. Pukhov, Z.M. Sheng, and J. Meyer-ter-Vehn, Phys. Plasmas **6**, 2847 (1999).

[14] M.I.K. Santala *et al.*, Phys. Rev. Lett. **84**, 1459 (2000).

[15] A. Antonetti *et al.*, Appl. Phys. B: Lasers Opt. **65**, 197 (1997).

[16] V. Malka, *Utilisation du Spectrometre d'Electrons à 200 MeV*, Note No. LULI-LOA, 1998.

[17] GEANT4, LCB Status Report No. CERN/LHCC-98-44, 1998 (unpublished).

[18] A. Veyssiere *et al.*, Nucl. Phys. A **199**, 45 (1973).

[19] T.J. Goldsack *et al.*, Phys. Fluids **25**, 1634 (1982); B. Yaakobi *et al.*, J. Appl. Phys. **57**, 4354 (1985).

[20] W.A. Lochstet *et al.*, Phys. Rev. **141**, 1002 (1961).

[21] V.V. Varlamov *et al.*, Yad. Konst. **2**, 3 (1995).

[22] A. Veyssiere *et al.*, Nucl. Phys. A **159**, 561 (1970).

[23] W.E. Stephens, Phys. Rev. **141**, 1002 (1966).

[24] H. Schwoerer *et al.*, Phys. Rev. Lett. **86**, 2317 (2001).

[25] C. Gahn *et al.*, Appl. Phys. Lett. **73**, 3662 (1998).

[26] E.L. Clark *et al.*, Phys. Rev. Lett. **85**, 1654 (2000).

[27] CALDER code, report (unpublished).

[28] C. Gahn *et al.*, Phys. Rev. Lett. **83**, 4772 (1999).

[29] V.T. Tikhonchuk, Phys. Plasmas **9**, 1416 (2002).